Serpentine geometry plasma actuators for flow control

Mark Riherd and Subrata Roy

Citation: J. Appl. Phys. **114**, 083303 (2013); doi: 10.1063/1.4818622
View online: http://dx.doi.org/10.1063/1.4818622
View Table of Contents: http://jap.aip.org/resource/1/JAPIAU/v114/i8
Published by the AIP Publishing LLC.

Serpentine geometry plasma actuators for flow control

Mark Riherd and Subrata Roy[a)]
Applied Physics Research Group, University of Florida, Gainesville, Florida 32611, USA

(Received 13 June 2013; accepted 1 August 2013; published online 23 August 2013)

In this paper, a curved class of plasma actuator geometries is presented. The intension of this paper is to extend the versatility of a dielectric barrier discharge plasma actuator by modifying the geometry of its electrodes, so that the plasma generated body force is able to excite a broader spectrum of flow physics than plasma actuators with a more standard geometry. Two examples of flow control are demonstrated numerically. An example of this class of actuators is shown to generate boundary layer streaks, which can be used to accelerate or delay the laminar to turbulent transition process, depending on how they are applied. Simulations of a low Reynolds number airfoil are also performed using additional examples of this class of actuators, where it is shown that this plasma actuator geometry is able to introduce energy into and excite a secondary instability mode and increase unsteady kinetic energy in the boundary layer. These two cases show that this general class of curved actuators possesses an increased versatility with respect to the standard geometry actuators. © *2013 AIP Publishing LLC*. [http://dx.doi.org/10.1063/1.4818622]

I. INTRODUCTION

As the demands for more efficient aircraft increase, so do the demands on the methods of flow control. Applications range from drag reduction during extended periods of cruising flight to separation control during take-off and landing. For many aircraft, the need for specific types of flow control varies over the course of a single flight, and the use of passive flow control actuators may be beneficial over some segments of the flight, but detrimental over other segments. As such, active flow control actuators[1] possess an advantage as they only influence the flow when electrical power is supplied to them.

As a method of introducing perturbations for low speed flow control, dielectric barrier discharge (DBD) actuators present themselves as a useful tool.[2,3] This type of plasma actuator has shown itself to be effective for boundary layer control[4–7] and for flow reattachment at low to moderate Reynolds numbers,[5,7–10] especially when used in a pulsed manner.

Plasma actuators with novel geometries, including the serpentine geometry, have been effective in a number of numerical studies[10–12] as well as some experimental work.[7,13,14] Specifically, the serpentine geometry actuators are able to introduce streamwise, as well as spanwise and surface normal vorticity to and promote increased mixing in the flow. The manner that three-dimensional perturbations can be introduced to the flow allows for an additional freedom when designing and implementing control. This additional degree of freedom may allow for greater control authority.

The present study aims to show the versatility of this class of actuators for exciting three-dimensional flow physics, and that under certain conditions, there are advantages to using serpentine geometry plasma actuators over the more traditional actuator geometries. Two examples are presented, highlighting different capabilities of this class of actuator.

The paper is organized as follows. In Sec. II, the serpentine geometry actuator is defined as a broad class of curved actuator geometries and is tied to existing actuator geometries, which have been reported in the literature. Brief characterization of the actuators under quiescent conditions is performed in Sec. III, along with some comparisons with previous experimental results,[14] before moving onto simulations of these actuators for flow control. In Sec. IV, serpentine geometry actuators are implemented in a laminar boundary layer in order to generate vortex streaks. The magnitude of the actuation is parametrically varied. Effects near the actuator are examined, and similarities are found with the quiescent flow simulations. Effects downstream of the actuator are also examined, and a linear response is noted for smaller levels of plasma actuation. A second example of flow control using these actuators in examined in Sec. V. In this case, the actuators are pulsed in order to introduce unsteady effects into a separated airfoil flow in order to control a laminar separation bubble. The geometry of the actuator is smoothly varied from a standard geometry actuator to a pronounced serpentine geometry actuator. Numerical measurements along the length of the airfoil indicate the serpentine geometry is capable of exciting two and three-dimensional instability modes, and accelerate the transition of the laminar flow. Finally, conclusions are drawn in Sec. VI.

II. SERPENTINE GEOMETRY DBD ACTUATORS

DBD actuators are devices consisting of two asymmetrically placed actuators separated by a dielectric material and exposed to a working gas on one side (Fig. 1(a)), while the other side was covered. One of the electrodes is grounded, while the other is normally operated with a sinusoidal voltage with a frequency of 1–50 kHz and amplitude of

[a)]Electronic mail: roy@ufl.edu

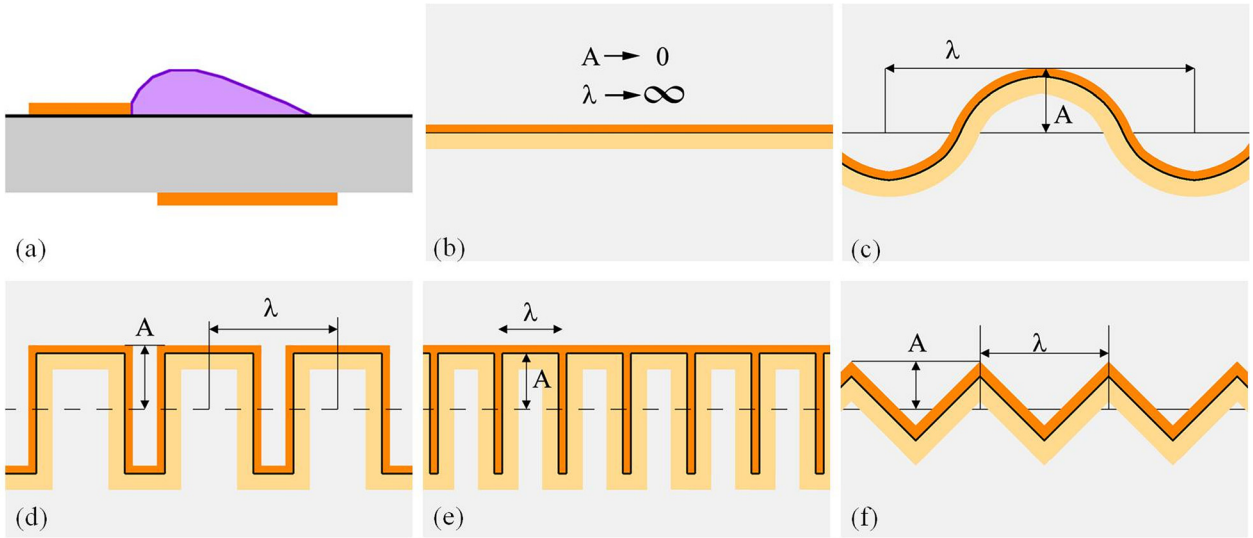

FIG. 1. (a) Schematic of DBD plasma actuator and the generated body force. (b) Linear, (c) arc, (d) rectangle, (e) comb/finger, and (f) triangle geometry serpentine actuators.

$5 - 60kV_{pp}$. The difference in electrical potential creates a significant electric field, which weakly ionizes the working gas in the immediate region. The combination of the electric field and charged particles induces a body force to the fluid, which can in turn be used for flow control applications.

A serpentine plasma actuator is characterized as a dielectric barrier discharge actuator where the electrodes are shaped such that they can be described by a continuous parametric function $(\vec{g}(s) = x(s)\hat{i} + y(s)\hat{j})$ that is periodic is some direction. Any serpentine geometries can be characterized as having a wavelength (λ) and an amplitude (A). If $x(s)$ and $y(s)$ are normalized such that $0 \leq x \leq 1$ and $-1 \leq y \leq 1$, the amplitude and wavelength of the actuation can be implemented such that $\vec{g}(s) = \lambda\hat{x}(s)\hat{i} + A\hat{y}(s)\hat{j}$. While the function itself is not constrained to be any specific shape, the existing scientific literature has only examined a geometries based on arcs (Fig. 1(c)), rectangles (Fig. 1(d)), combs/fingers (Fig. 1(e)), and triangles (Fig. 1(d)),[7,10,12,14] though nearly any shape could be implemented. As such, the serpentine geometry can be considered to be a general class of actuators.

Included in this class of actuator geometries is the linear geometry actuator (Fig. 1(b)). This geometry consists only of the two electrodes stretching out infinitely far in some direction with no periodic variation, and can be reached in the limit of $\lambda \to \infty$ or as $A \to 0$. The linear geometry is a special case of the serpentine geometry, as it does not have any periodic variation, and will only introduce a two dimensional perturbation, while the other geometries produce three dimensional perturbations. This is an important distinction to make as the inclusion of three dimensional perturbations can have a significant impact on the flow control mechanisms at work.

A second special case is that of the comb/finger geometry.[7] This geometry can be defined as when the electrodes in two adjacent half wavelengths merge together. For all geometries included in this subset, periodic electrodes are all connected such that they form a single actuator (Fig. 1(e)). There are implications of this with respect to the installation and manufacturing of these devices, the applicable flow control mechanism, and also with the electrical properties of the actuator.

III. ACTUATOR BEHAVIOR UNDER QUIESCENT CONDITIONS

Prior to applying this class of devices for flow control, it should be determined how these devices behave under quiescent conditions. Knowledge of this behavior should provide insight into how these devices perturb a flow. This class of devices has been previously studied in order to determine how they behave under quiescent conditions.[12,14] The purpose of presenting these data here is two-fold. These data are presented in order to show qualitative agreement between the existing experimental measurements and the present calculations. These data are also presented in order to provide insight on how these devices could be useful for specific flow control applications.

A. Numerical details

In order to simulate these flows, the Implicit Large Eddy Simulation (ILES) Navier-Stokes solver, FDL3DI (Ref. 15) is employed. This code solves the compressible, three-dimensional Navier-Stokes equations. While this code is solving the compressible form of the Navier-Stokes equations, an incompressible flow can be solved by setting the freestream Mach number, M_∞, to an appropriately low value. It has been determined that a value of $M_\infty = 0.1$ provides a reasonable balance of incompressibility and numerical stability,[15] though the actual Mach numbers in the flow are between 0.01 and 0.05. In the present simulations (performed at this Mach number), variations to the fluid density are found to be less than 1% throughout the domain, indicating that the flows are essentially incompressible.

Dimensional and non-dimensional parameters can be found in Table I. The effects of plasma actuation are

TABLE I. Dimensional and non-dimensional values used to compute the base flow.

Reference parameter	Value
Dimensional values	
u_∞	5 m/s
L	0.3 m
ρ_∞	1.20 kg/m^3
ν	1.5×10^{-5}m^2/s
Non-dimensional values	
Re	100 000
Pr	0.72
Ma	0.1
D_c	varies, see Fig. 3

modeled using an approximate body force distribution (Fig. 2(b)) based on first principles simulations of the plasma discharge[16] and applied along the edge of the exposed electrode (Fig. 2(c)) in a manner consistent with the description in Rizzetta *et al.*[15] This body force distribution is described as

$$f_x = \frac{F_{x,0}}{\sqrt{F_{x,0}^2 + F_{y,0}^2}} \exp\left(-\left(\frac{(x-x_0)-(y-y_0)}{y-y_0+y_b} \right)^2 - \beta_x (y-y_0)^2 \right), \quad (1)$$

$$f_y = \frac{F_{y,0}}{\sqrt{F_{x,0}^2 + F_{y,0}^2}} \exp\left(-\left(\frac{x-x_0}{y-y_0+y_b} \right)^2 - \beta_y (y-y_0)^2 \right), \quad (2)$$

where $F_{x,0} = 2.6$, $F_{y,0} = 2.0$, $\beta_x = 7.2 \times 10^4$, $\beta_y = 9 \times 10^5$, and $y_b = 0.00333$. x_0 and y_0 represent the edge location of the electrodes. While this body force lacks the accuracy of a fully coupled simulation of the plasma and fluid dynamics, it is more accurate than phenomenological models. This approach also avoids the expensive computations required of a fully coupled simulation. The plasma actuation is modulated through a non-dimensional parameter, D_c, which relates the magnitude of the body force to the dynamic pressure (i.e., $D_c = \frac{|f_0|}{\rho u_\infty^2}$).

For these simulations, the flow was simulated in a three dimensional box of size [0.3, 8.0] × [0, 1.5] × [0.0, 0.1] in the $x \times y \times z$ directions. The grid used to resolve the mesh contains ≈7.5 million grid points (763 × 151 × 65 points in the $x \times y \times x$ directions). The mesh is highly refined at the inlet and around and downstream of the actuator ($\Delta x = 0.001$ for $1.0 < x < 1.1$ and smoothly stretches to $\Delta x = 0.01$ for $1.6 < x < 4.0$). The mesh is also refined near the wall ($\Delta y_{wall} = 0.0002$). Far away from the wall and downstream of the actuator, the mesh is geometrically stretched. Δx is stretched by 6.1% for $x > 4$, and Δy is stretched by 9.7% for $y > 0.04$ (roughly four times the height of the plasma body force). This stretching is done to minimize the number of grid points necessary, as well as to prevent reflections off of these boundaries. A uniform mesh spacing is used in the spanwise direction, where $\Delta z = 0.0015625$. This spacing provides 64 points to resolve a single wavelength ($\lambda = 0.1$) of the plasma actuator, which should be more than sufficient for the effects at the primary and first few harmonics of this wavelength. At this resolution, the plasma actuator is resolved by 40 points in the wall normal direction, and 20 to 30 points in the z to x directions, depending on the orientation of the body force along the length of the serpentine geometry.

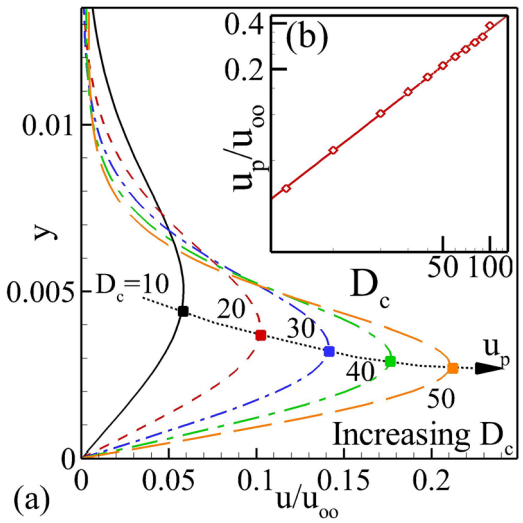

FIG. 3. (a) Velocity profiles at a location downstream of the plasma actuation for various values of D_c under quiescent conditions. (b) Values of u_p used to calibrate D_c.

For boundary conditions, no slip conditions are applied at the inlet ($x = 0.3$) and the wall surface ($y = 0.0$), while a no shear boundary condition is applied for the far field ($y = 1.5$) and outlet ($x = 8.0$) boundaries. The mesh and its boundary conditions are shown in Fig. 2.

The serpentine geometry plasma actuator is centered at $x = 1.025$. The streamwise amplitude of the serpentine

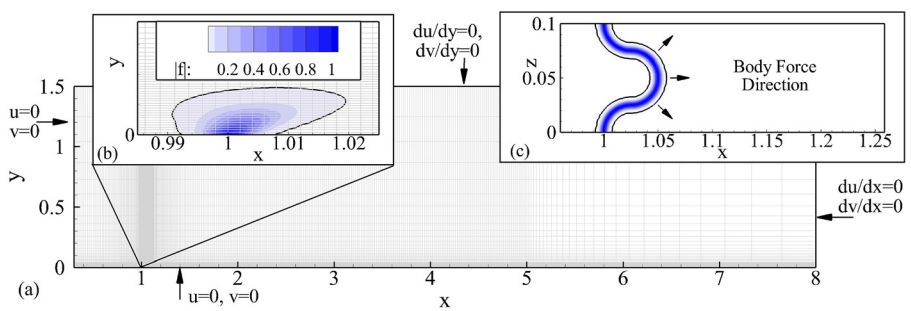

FIG. 2. (a) Mesh, (b) two-dimensional slice of the body force (at $z = 0$), and (c) top view of the geometry used to simulate the serpentine geometry plasma actuation. Every other point is shown. The black lines in (b) and (c) refer to where the body force is 1% of the maximum body force.

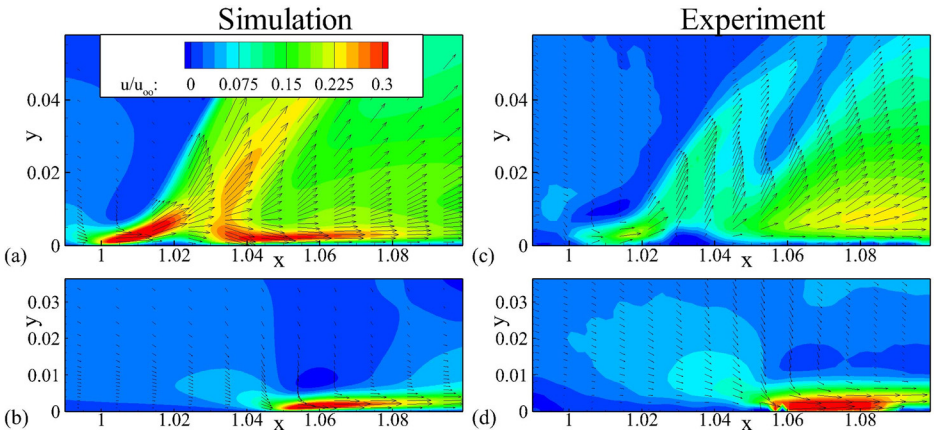

FIG. 4. Velocity fields at the ((a) and (c)) pinch point ($z=0$), ((b) and (d)) spreading point ($z=0.05$) of the serpentine geometry actuator operated under quiescent conditions for ((a) and (b)) simulations with a prescribed induced velocity of $u_p/u_\infty = 0.1$ and ((c) and (d)) experiments performed by Durcher and Roy.[14] The experimental results have been non-dimensionalized so that the relative sizes of the actuators match.

geometry is $A=0.025$, so the leading edge of the actuator geometry is located at the point $x=1$. The trailing edge of the actuator geometry is centered at $x=1.05$. The spanwise wave length of the actuator geometry is $\lambda = 0.1$. This geometry is equivalent to the one shown in Fig. 1(c).

In order to characterize the magnitude of the body force in terms of an induced flow velocity, two-dimensional simulations of a linear geometry plasma actuator using an identical body force and a two-dimensional mesh have also been performed under quiescent conditions, varying the strength of the plasma actuator though the use of the non-dimensional parameter D_c. The induced flow is then characterized by the maximum velocity generated by the body force under quiescent conditions at a downstream point (u_p, Fig. 3).

For the present case, the flow is examined at a point 0.0333 units downstream of the center of the body force (i.e., $x=1.033$ in Fig. 2(b)). The data from these simulations are then used to determine the values of D_c to use to generate a body force capable of producing a wall jet with the specified velocity of u_p. In the non-quiescent simulations, the magnitude of the plasma actuation is defined through the non-dimensional velocity ratio γ_0, where γ_0 is the ratio of the plasma induced wall jet velocity under quiescent conditions over the free stream velocity (i.e., $\gamma_0 = \frac{u_p}{u_\infty}$).

B. Characteristic flow features

Examining the flow fields around the serpentine geometry actuators operated under quiescent conditions, it can be seen that several interesting flow features are present (Fig. 4). These results are shown alongside stereographic particle image velocimetry (PIV) results of a comparable experiment performed by Durcher and Roy[14] for a comparable experiment (Figs. 8(a) and 8(b) of Durcher and Roy[14]), and show good qualitative agreement. At the pinch point, a vectored jet is produced (Fig. 4(a)). This contrasts with the much simpler behavior at the spreading point of the actuator geometry, where a simple wall jet has formed (Fig. 4(b)). A twisted vectored jet is visualized using streamlines in Fig. 5(a), which compared favorably to experimental results in Fig. 5(b). In these streamlines, the effects of a streamwise oriented vortex can be seen downstream of the actuator (identified by the twisting braid of streamlines). The streamwise oriented vorticity in the flow field can be more clearly seen in Fig. 6. As these flows have been discussed by Wang *et al.*[12] and Durscher and Roy[14] and are in qualitative agreement with those studies, so they will not be discussed in further length.

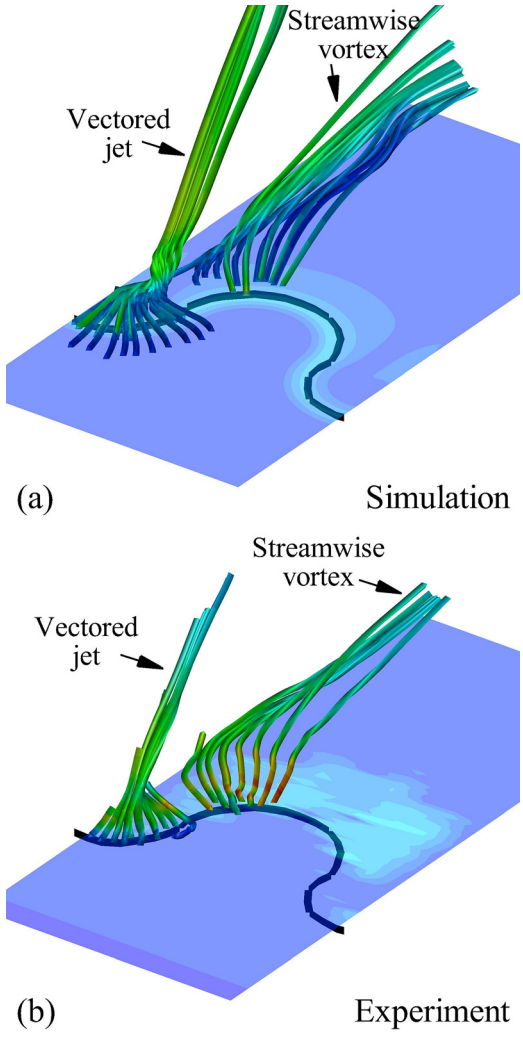

FIG. 5. Streamlines in the flow fields from the (a) simulation of a $u_p/u_\infty = 0.1$ serpentine actuator and (b) experiments for a curved serpentine actuator. A black line is used to indicate the location of the actuator. Experimental data from Durscher and Roy.[14]

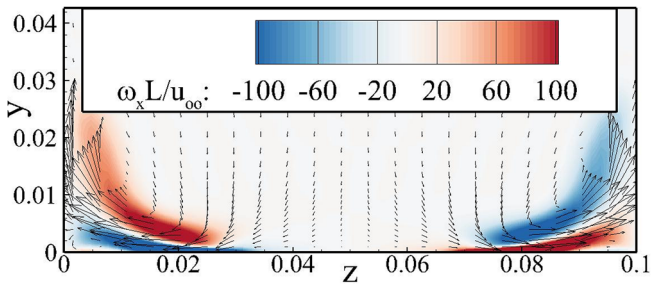

FIG. 6. Streamwise vorticity at $x = 1.025$ of the serpentine geometry actuator operated under quiescent conditions for simulation with a prescribed induced velocity of $u_p/u_\infty = 0.1$.

IV. APPLICATION TO A LAMINAR BOUNDARY LAYER

One potential application of the serpentine geometry actuators is to use them to generate boundary layer streaks. These streaks are a type of transient instability mechanism that is capable of achieving very large energy growth over finite time scales,[17] are initiated by streamwise vorticity, and are a common path to transition in the presence of free stream turbulence.[18,19] When they reach a large enough magnitude, these streaks can become unstable and can lead to the flow becoming turbulent.[20] However, there is experimental evidence suggesting that if they are introduced to the flow in a controlled manner and at a low enough magnitude, they can be used to stabilize the flow instead.[21]

Serpentine geometry actuators can produce streamwise oriented vorticity, so it should be possible to use them to introduce controlled streaks to a flow. In applying this manner of actuation, it should be possible to control the amplitude of the streaks in such a manner to stabilize (low magnitude streaks) or destabilize (higher magnitude streaks) the flow in order to achieve the desired effect downstream of the actuator. As such, if the streak magnitude can be actively controlled, then it would allow for a single actuator to accelerate or delay the onset of turbulence, depending on how it is operated.

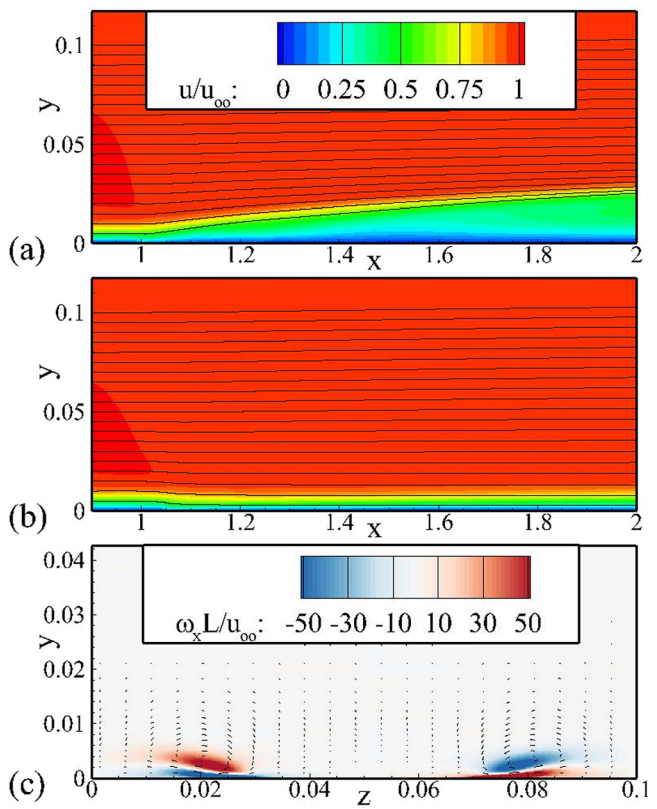

FIG. 7. Comparisons of the velocity field near the plasma actuator for the velocity ratio $\gamma_0 = 0.05$ in a boundary layer flow. The (a) pinching and (b) spreading points are shown, along with the (c) streamwise vorticity at $x = 1.025$. Note that the x and y scales are not equal in (a) and (b).

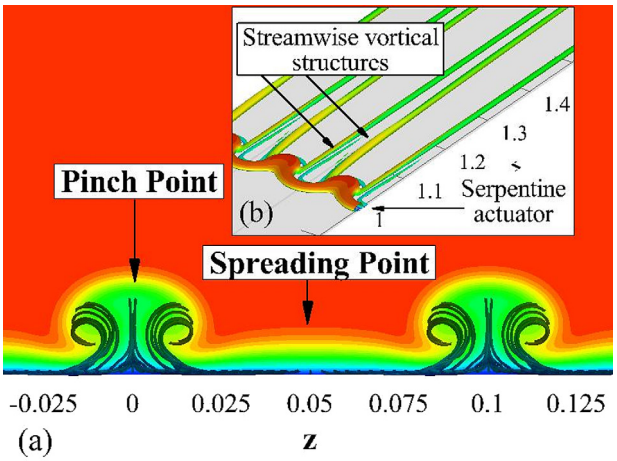

FIG. 8. (a) Streamtraces (with a background of the u velocity at $x = 1.5$) and (b) Q-criteria (colored by velocity magnitude) for the case of $\gamma_0 = 0.05$ in a boundary layer flow. The data set is repeated twice more in the z-direction, only a single wavelength was simulated.

Simulations have been performed in order to examine the effects of a serpentine actuator in a laminar boundary layer. These simulations are based around flow conditions at relatively low Reynolds numbers, where the actuator is placed at a streamwise Reynolds number of $Re_x = 100\,000$. These simulations are perturbed (though not in any active manner) by a steady addition of momentum to the flow through the plasma body force. At the actuator location, the displacement boundary layer height is $\delta_0^* = 0.00544$, the 99% boundary layer height is $\delta_{99\%} = 0.0158$, the boundary

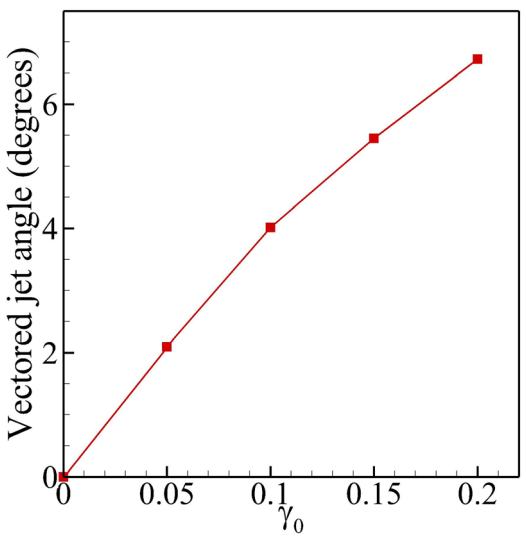

FIG. 9. Angle of the vectored jet as the velocity ratio is varied. This angle was measured as the maximum flow angle at the height of $y = \delta_0^* = 0.00544$ downstream of the pinching point.

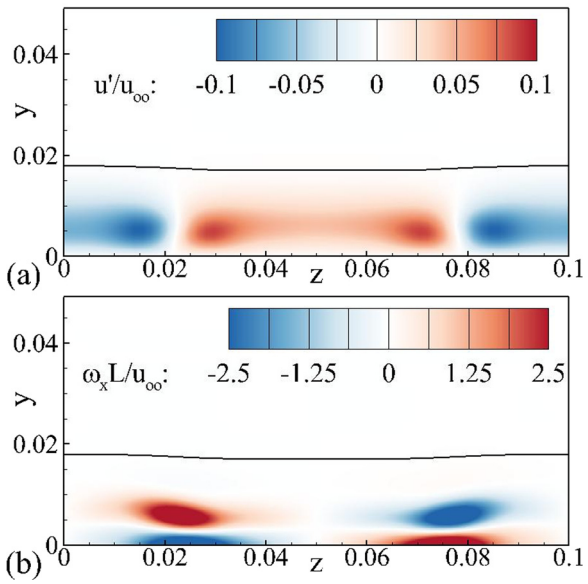

FIG. 10. Streamwise variations in the (a) velocity magnitudes and (b) streamwise vorticity at $x = 1.2$ for the case of $\gamma_0 = 0.01$. The 99% boundary layer height ($\delta_{99\%}$) is marked by the thick solid line.

layer Reynolds number is $Re_{\delta^*} = 544$, and one unit of length is approximately $180\delta_0^*$.

For these simulations, the same mesh as used in the quiescent simulations is employed. The resolution of different flow features in the boundary layer is similar to that of the flow features in the quiescent simulations, with the additional constraints that the boundary layer also be well resolved. To that effect, there are 28 points within the displacement boundary layer height and 70 points within the 99% boundary layer height at $x = 1$, which should be more than enough to simulate the effects of a serpentine plasma actuator in a laminar boundary layer.

A. Characteristic flow features

The modified flow fields possess several flow features that are due to the introduction of serpentine geometry plasma actuation. The first of these is the forcing of fluid away from the surface in the region immediately downstream of the actuator in a vectored jet, comparable to the effects of a plasma synthetic jet[13] (Fig. 7(a)). The second of these is the counter rotating streamwise oriented vortices that propagate downstream[11,14] (Figs. 7(c) and 8). Both of these effects have been previously reported in the existing literature for serpentine actuator driven flows under quiescent conditions[12,14] and in laminar boundary layers.[11]

Examining the flow field at the pinch point of the actuator (Fig. 7(a)), it can be seen that the vectored jet produced in the presence of a mean flow is of a shallower angle than that produced under quiescent conditions (typically in the range of 40° to 50°[14]). The angle of the jet is strongly dependent on the magnitude of the plasma actuation, where a larger velocity ratio produces a steeper jet (Fig. 9). Importantly, the presence of this vectored jet indicates that the effects of actuation are able to penetrate into the bulk flow. At the spreading point (Fig. 7(b)), fluid is entrained towards the surface by the body force, an effect that has been seen for standard geometry plasma actuators in boundary layers previously.

Upon examination of the serpentine plasma actuated boundary layer, it is found that the streamwise velocity variations (where $u' = u - \bar{u}$, Fig. 10(a)) qualitatively match those of the optimally growing boundary layer streaks, including the large difference between the streamwise and wall normal/spanwise velocity components. For lower levels of actuation, there appears to be reasonable qualitative agreement between the shape and structure of the generated streaks and the optimally generated streaks described for the Blasius boundary layer by previous researchers.[17,18] However, for higher velocity ratios ($\gamma_0 \geq 0.05$), the qualitative agreement becomes weaker as non-linear effects deform the streaks. Even so, this type of behavior in the flow suggests that the serpentine plasma actuator is able to generate boundary layer streaks.

Examining the perturbation velocity profiles of the generated boundary layer streaks, it appears that the plasma actuation generates effects comparable to the optimal boundary layer for smaller levels of plasma actuation (where the streak velocity profile is defined at the standard deviation of the streamwise flow velocity across the span of the boundary layer, Fig. 11). For lower levels of actuation, the streak velocity profiles display the expected smooth shape, with a

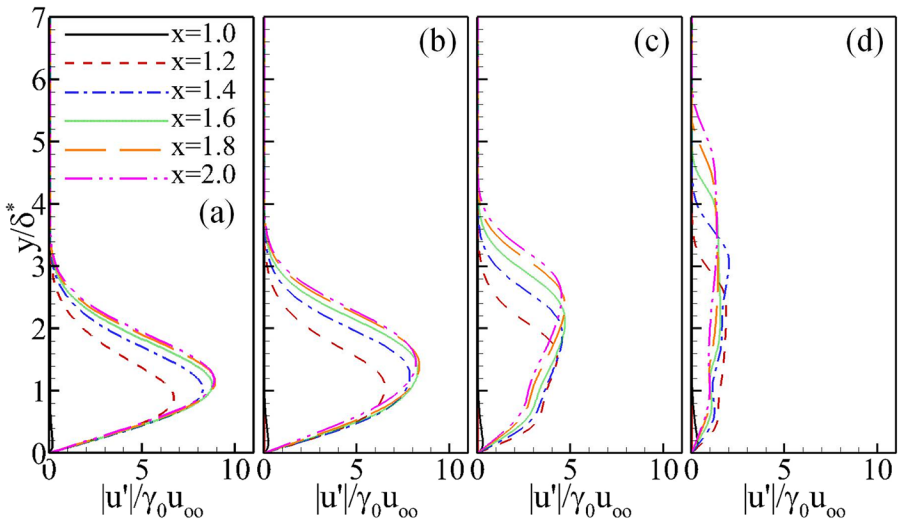

FIG. 11. Normalized boundary layer streak profiles based on the standard deviation of the streamwise velocity across the span of the boundary layer for (a) $\gamma_0 = 0.01$, (b) $\gamma_0 = 0.025$, (c) $\gamma_0 = 0.05$, and (d) $\gamma_0 = 0.10$.

peak velocity at approximately the same height as the displacement boundary layer height, which is expected based on previous studies.[17,18] However, as the magnitude of the actuation is increased, non-linear effects become important, and the effect of the body force on the boundary layer no longer resembles the intended boundary layer streaks.

Defining the streak velocity magnitude as half the difference between the velocity at the center of the high (i.e., the spreading point, z = 0.05) and low speed streak (i.e., the pinch point, z = 0.00) regions,

$$A_u(x) = \max_{y\in[0,\infty)} \frac{|u_{pinch}(x,y) - u_{spread}(x,y)|}{2u_\infty}, \quad (3)$$

and the streamwise vortex magnitude as the total amount of vorticity along the length of the boundary layer,

$$A_{\omega_x} = \int_{z=0}^{\lambda}\int_{y=0}^{\infty} |\omega_x| dydz, \quad (4)$$

the magnitude of the streaks can also be quantified (Fig. 12). In applying these metrics, it can be seen that magnitude of the vortex streak scales nicely with respect to the velocity ratio γ_0 until non-linear effects become important. It appears that streak velocity magnitude can be amplified an order of magnitude larger the induced velocity of the plasma actuation. This amplification should also be a function of the spanwise wave number and the Reynolds number of the flow, effects not examined in the present study. The magnitude of the streamwise oriented vorticity seems to be more robust against non-linear effects, and appears to scale nicely with respect to $\gamma_0^{1/2}$ even once non-linear effects have set in.

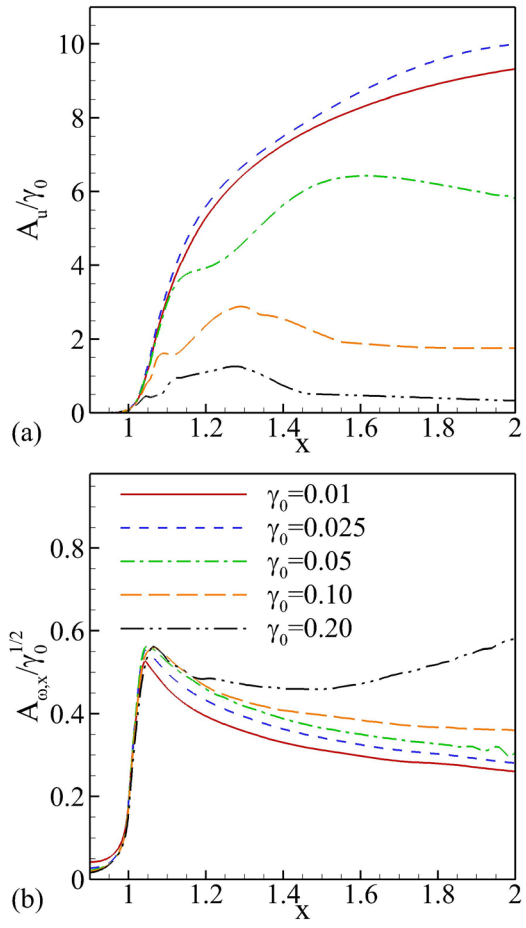

FIG. 12. Normalized boundary layer streak (a) velocity magnitude and (b) streamwise vortex magnitude.

V. APPLICATION TO A LAMINAR SEPARATED FLOW

One common application of plasma devices is for the control of separated flows.[5,7,10,22] In a laminar flow separation, a laminar boundary layer separates due to an adverse pressure gradient. The control of these flows is typically performed by introducing periodic excitations upstream of the laminar separation bubble.[23] These excitations are able to remove the flow separation and maintain flow attachment by increasing the near wall momentum due to additional unsteady mixing in the boundary layer, which helps the fluid to overcome the adverse pressure gradient. Thus, if the unsteady mixing were to be further increased, then the flow could be made more robust against more adverse pressure gradients.

In this case, using the modified shape of the serpentine geometry actuators, perturbations are introduced to the flow which will increase the amount of unsteady mixing in the boundary layer. Doing so should result in a more robust application of control for laminar separated boundary layers.

A. Numerical details and data collection

The flow of interest is that around an SD7003 airfoil operated at a chord based Reynolds number of 40 000 and an angle of attack of 4°. This particular airfoil, Reynolds number, and angle of attack are representative of the flow for a low speed unmanned air vehicles (UAV) applications, but the application of control under low speed applications may lead to improved flow control for larger vehicles at higher velocities.

Simulations are performed on a cylindrical O-mesh of 390 × 242 × 92 (angular × radial × spanwise) points representing an SD7003 airfoil with a unit chord length (Fig. 13) and extended 0.2 chord lengths (c) in the spanwise direction. The mesh extends radially outwards 100 chord lengths in order to provide a good free stream condition (with no free stream turbulence present). The mesh is also stretched as it extends to the free stream in order to prevent reflections off of the free stream boundary. Periodic boundary conditions were applied in the spanwise and angular directions. With respect to the resolution of the mesh near the airfoil, the grid spacing along the length of the airfoil is ≈0.001 near the plasma actuator, and at no point along the suction side of the airfoil is the grid spacing greater than 0.0075. In the wall

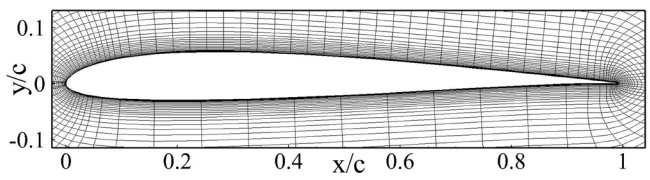

FIG. 13. Grid used to perform simulations around an SD7003 airfoil. Every fourth grid point is shown.

normal direction, the grid spacing is approximately 0.0005 along the length of the airfoil. In the spanwise direction, the mesh spacing is uniform, where $\Delta z = 0.002174$. In the simulations performed with plasma control, the characteristic wavelengths of the resulting disturbances are $\lambda_x \approx 0.1$ and $\lambda_z = 0.05$. As such, this indicates that the perturbations generated by the control are resolved by a minimum of 13 grid points in the streamwise direction (and often many more where the grid resolution is denser) and 46 grid points in the spanwise direction. This suggests that the primary perturbations generated by the plasma control should be supported by the mesh, as well as the first few harmonics. While this grid resolution may not be able to resolve the smaller, dissipative scales of any turbulent flow features, the effects of control on the earlier stages of turbulence should still be resolved. The baseline flow case was also simulated on a mesh with 650 × 390 × 151 points representing the same domain in order to check for grid independence of the solution. The flow field was found to be independent of mesh resolution.

A time step of $\Delta t = 0.0001$ is used for the majority of the simulations, but higher ($2\Delta t$) and lower ($\Delta t/2$) time steps are also examined for the baseline case. Results shown in Fig. 14(d) ensure independence of temporal resolution for $\Delta t \leq 0.0001$. Each simulation of the flow around an airfoil is run for 5 units of non-dimensional time ($t_0 = c/u_\infty$) in order to remove any transient effects and then for 5 additional units of non-dimensional time in order to collect statistics. Values of u, v, and w are collected along 39 spanwise lines with a spacing of $0.025c$ near the surface at every time step in order to provide sufficient data for spectral analysis across the span and in time. Fourier transforms are performed in order to examine the energy content of velocity fields at specific spanwise and temporal frequencies (Eq. (5)), allowing the power spectral densities (PSD) of the kinetic energy to be calculated (Eq. (6))

$$\tilde{u}(x,k,f) = \frac{1}{t_{max} z_{span}} \int_0^{t_{max}} \int_0^{z_{span}} u(x,z,t) \exp(i2\pi(kz - ft)) dz dt, \tag{5}$$

$$PSD(x,k,f) = \frac{1}{2}(\tilde{u}\tilde{u}^* + \tilde{v}\tilde{v}^* + \tilde{w}\tilde{w}^*), \tag{6}$$

where (*) denotes the complex conjugate.

The Q-criterion is used to identify vortical structures in the simulated flow fields.[24] For all of the figures where the Q-criterion is shown, a value of $Q = 100$ is used to illustrate the presence of vortical structures. The value of $Q = 100$ was selected as it is still small compared to the maximum value of Q for the flow field (≈1%), and the iso-surfaces are relatively insensitive to the value of Q.

B. Characteristics of the baseflow around and SD7003 airfoil

The baseline flow with no actuation around the airfoil can be classified as having a laminar separation bubble (Figs. 14(a) and 14(b)). The freestream flow initially moves laminarly around the airfoil. It separates roughly a quarter chord downstream of the leading edge. Disturbances grow within the separation region and create very weak vortical structures to form on the upper portion of the separation bubble, which can be considered similar to a free shear layer. At approximately $x/c = 0.75$, the flow rapidly transitions to turbulence; and due to the increased momentum transfer from the vortical structures in the shear layer, the flow reattaches (Figs. 14(a) and 14(b)). These flow field results match up well with previous numerical and experimental studies[25,26] at similar conditions.

The shedding of vortical structures within the laminar separation bubble suggests that there is an instability present that may be of use for controlling this flow.[10] The power spectral densities of the flow at the mid chord ($x/c = 0.5$) and near the trailing edge ($x/c = 0.9$) show that there are unsteady effects focused at the frequency $St = 5.0$ (Fig. 14(c)). Furthermore, the lack of unsteady behavior at the mid-chord at frequencies other that $St = 5.0$ indicates that this flow is largely still laminar/transitional, while the wider frequency band of unsteady effects near the trailing edge shows that the flow has become turbulent at that point.

Furthermore, as a comparison to results that will be shown later, the growth of certain unsteady modes is also presented. The modes are separated by their respective spatial and temporal frequencies. The (k,h)th mode refers to the k-th multiple of the characteristic spanwise frequency and the h-th multiple of the characteristic temporal frequency, i.e., the (0,0) mode refers to effects that are constant across the span and steady in time, the (1,1) mode refers to mode which is excited at the characteristic spanwise wavelength

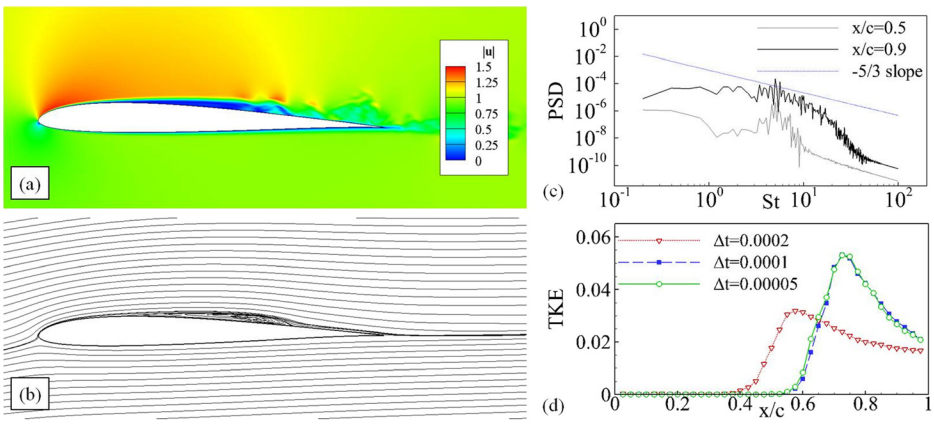

FIG. 14. (a) Instantaneous velocity magnitude $|u|$ and (b) streamlines of the baseline separated flow. (c) Power spectral densities of the turbulent kinetic energy for the baseline separated flow at the mid chord and near the trailing edge. (d) Turbulent kinetic energy along the surface of the airfoil for varying Δt.

and frequency, and the (3,2) mode would refer to the second harmonic across the span and the first harmonic of the fundamental frequency. The fundamental spanwise frequency is $10/c$ and the Strouhal number of the forcing is $St_0 = 5.0$.

The primary growing mode in the uncontrolled case is the (0,1) mode (Fig. 15), which represents a spanwise constant effect in the velocity field at a Strouhal number of $St = 5.0$. This particular mode corresponds to a periodic vortex shedding in the separated flow region. The other unsteady, spanwise constant mode shown, (0, 2), also has a finite amplitude larger than other modes of the same frequency. This indicates that two-dimensional effects are dominant until the separated flow region transitions and breaks down. Examining the three-dimensional modes in Fig. 15, they all show similar magnitudes and growth rates within the circulation region and saturate in amplitude, once the flow has transitioned. The similar rate that all of these modes grow and saturate at suggests that this laminar separation bubble transitions rapidly to produce a broad spectrum of effects, which is consistent with the flow and PSD data shown in Figs. 14(a)–14(c).

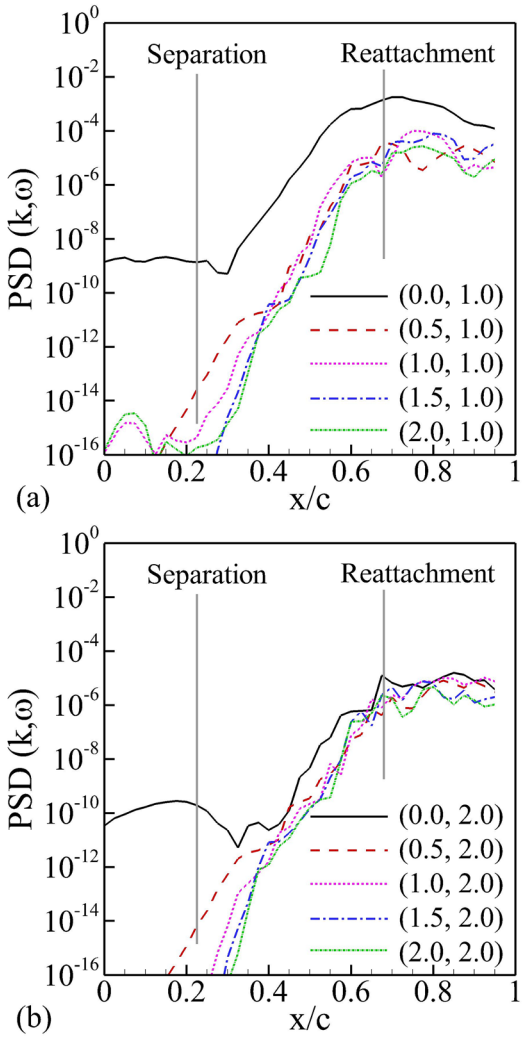

FIG. 15. Kinetic energy contained in Fourier modes across a number of temporal and spatial frequencies for the baseline separated flow. (a) $St = 5.0$ and (b) $St = 10.0$ effects are shown. Separation and reattachment points are marked.

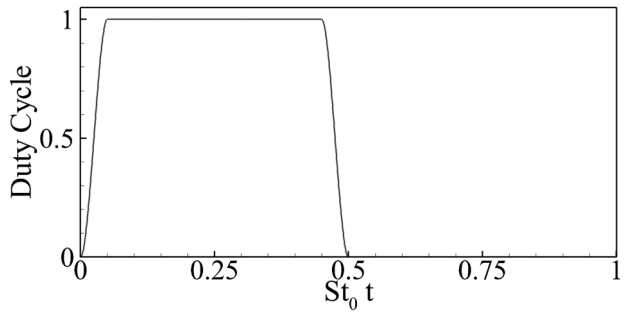

FIG. 16. Duty cycle applied to the plasma body force over a cycle of forcing.

C. Controlling the flow

As part of this study, the plasma was pulsed using a 45% duty cycle. The duty cycle was smoothed using a piecewise cubic polynomial between the on and off states such that no temporal discontinuities were introduced to the flow (Fig. 16). Four different serpentine plasma actuators were simulated for this study, varying the geometric amplitude of the geometries (Fig. 17). Parameters of these geometries can be found in Table II.

1. Application of a standard geometry actuator

With the addition of small unsteady disturbances from a standard geometry plasma actuator operated in a counterflow manner, the flow can be fully reattached,[10] which is indicated by no remaining separation bubble. These small disturbances generate Tollmien-Schlichting (TS) wave-like vortices to be shed from the actuator as it is duty cycled. In turn, these TS wave-like induce momentum transfer from the freestream into the boundary layer, eliminating the flow separation.

Examining the power spectral density at the mid-chord and near the trailing edge of the airfoil (Fig. 19(a)), the

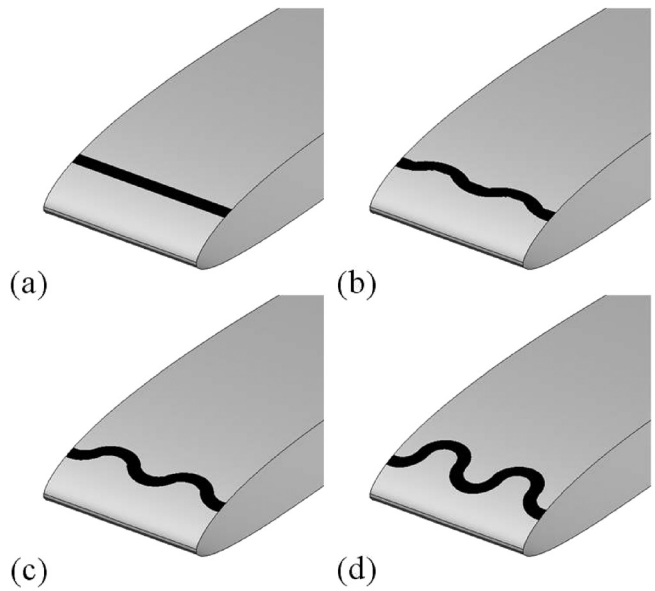

FIG. 17. Geometries of the actuators tested. (a) Linear. (b) Quarter serpentine. (c) Half serpentine. (d) Full serpentine.

TABLE II. Details of the plasma actuator geometries.

Force geometry	Amplitude (A)	Wavelength (λ)	Center of actuator (x/c)
Full	0.02500	0.1	0.06086
Half	0.01250	0.1	0.06086
Quarter	0.00625	0.1	0.06086
Linear	0.0	n/a	0.06086

unsteady energy in the flow is largely concentrated into isolated peaks, corresponding to the fundamental excitation frequency and its harmonics. This is a change from the case of no control, as it indicates that the energy has moved out of the quasi-periodic vortex shedding that occurred with the laminar separated flow (Fig. 14(d)) and into the regular, periodic vortex shedding that occurs due to the excitation of the actuator.

Comparing the magnitudes of the various Fourier mode components as the propagate downstream over the surface of the airfoil, fundamental differences can be seen between this case (Fig. 19(b)) and the case with no plasma actuation (Fig. 15(a)). Energy is actively added into the flow through the (0,1) mode at the actuator location. Though some energy is immediately lost due to receptivity effects, this mode eventually begins to grow, indicating that a natural flow instability has been excited.

However, this TS wave-like structure appears to possess its own secondary instability properties as it breaks down. Beginning at $x/c \approx 0.6$, spanwise variations in the flow start to appear (Fig. 18(b)), and the magnitude of the TS wave-like perturbation seems to saturate. At this point in the flow, the TS wave begins to become more sinuous in shape. The power spectral density of these spanwise varying modes (i.e., (1,1) and (2,1) in Fig. 19(b)) show that a slow, but nearly constant exponential growth of these perturbations as they are convected over the surface of the airfoil. By the time they reach the mid-chord, these spanwise perturbations to the flow become large enough to be non-negligible. As these spanwise variations grow, it appears that the transition of the flow accelerates as it moves closer to the trailing edge of the airfoil.

The introduction of small spanwise disturbances is critical to the breakdown of the primary vortical structure. There are no intentional sources of spanwise variation in the flow field which could provide a source of weakly non-linear growth. Ruling out that option, the breakdown of these vortices is likely due to small disturbances (either numerical or physical) exciting a secondary instability mode.

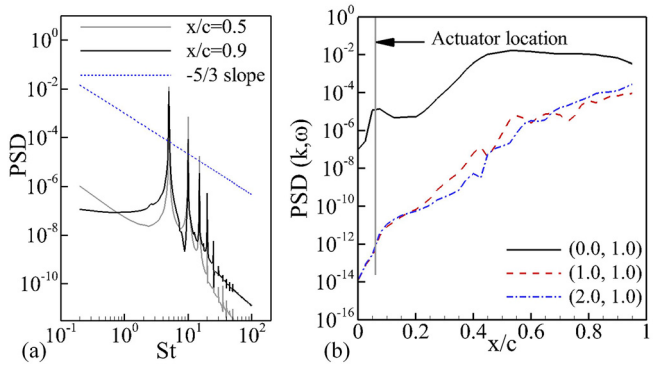

FIG. 19. (a) Power spectral densities of the turbulent kinetic energy and (b) magnitudes of the fundamental frequency (St = 5.0) modes across a number spatial frequencies for the flow actuated by the linear actuator.

2. Application of serpentine geometry actuation

The addition of spanwise variations to the flow control device adds another degree of freedom to the flow control mechanism. Earlier studies by Rizzetta and Visbal showed very distinct changes in the structures shed by the duty cycled plasma actuator when the geometry was changed to a very full serpentine geometry.[10] Those studies showed that when pulsed, the serpentine plasma actuators produced very complex vortical structures, which quickly broke down to produce a highly turbulent flow. In order to examine the effects of moving from a purely two dimensional control mechanism (the standard geometry) to a three dimensional flow control mechanism, a very slight amount of spanwise variation can be introduced to the body force (such as in the quarter serpentine geometry).

Just as with the case of the linear geometry actuator, the application of the pulsed serpentine geometry actuator results in complete reattachment of the flow. However, there are differences in the transition occurring downstream of the actuator. In examining the effects of only implementing a slight spanwise variation to the flow control (Figs. 20(a)–20(c)), the laminar to turbulent transition of the flow is still quite rapid. The initial vortices shed by the actuator have a similar shape as those of the linear actuation, but a sinuous spanwise variation is visible, an effect most easily seen from a top view of the flow (Fig. 20(b)). Furthermore, the breakdown of this vortex occurs much more quickly, and begins to occur around the mid-chord of the airfoil. As the geometry of the actuation becomes more pronounced, these effects are amplified, and three-dimensional effects become

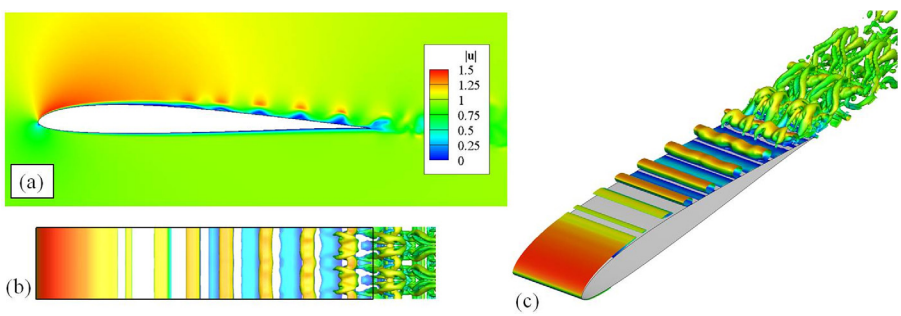

FIG. 18. (a) Instantaneous velocity magnitude and ((b) and (c)) Q = 100 iso-surfaces (colored by the velocity magnitude) for the linear geometry actuation as viewed from the (b) top and (c) iso-metric perspectives.

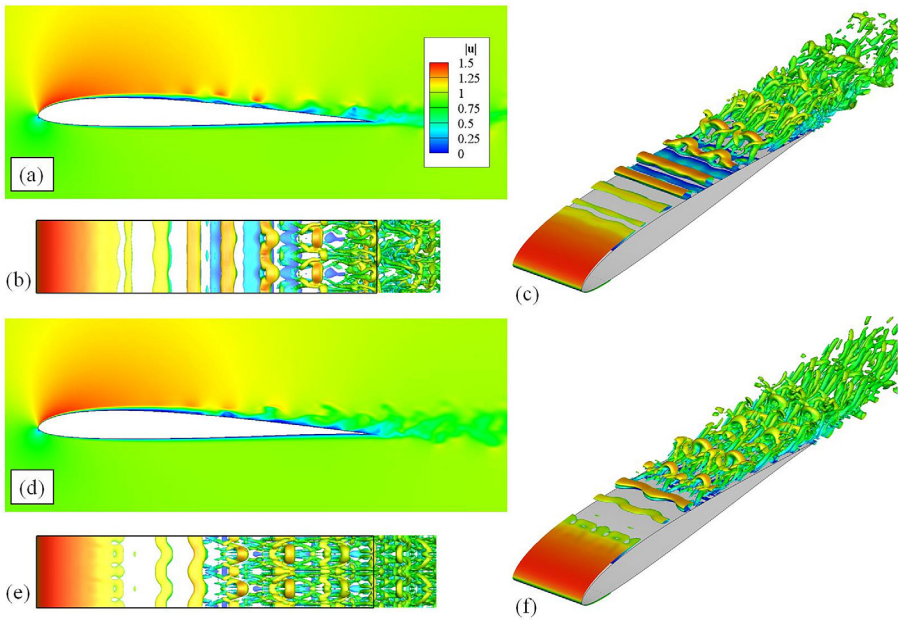

FIG. 20. ((a) and (d)) Instantaneous velocity magnitude and vortical structures as viewed from the ((b) and (e)) top and ((c) and (f)) iso-metric perspectives. The vortical structures are visualized through the Q-criterion, Q = 100, and colored by the velocity magnitude for the ((a)-(c)) quarter and ((d)-(f)) full serpentine geometries.

prominent closer to the leading edge of the airfoil (Figs. 20(d)–20(f)).

Tracking the growth of selected Fourier modes, it can be seen that the spanwise modes, which are negligible for the linear actuation until breakdown of the primary spanwise vortical structure occurs, are now very significant. For the quarter serpentine geometry, all of the tracked modes are inserted to some degree where the actuator is located (Fig. 21). The perturbation energy is largely injected into the (0,1) and (1,1) modes, but energy is supplied into other modes as well due energy spilling out of the duty cycle and the actuator geometry, as neither are perfectly sinusoidal.

Comparing the modes across the range of actuator geometries simulated, when the body force is applied to the flow, it appears that the magnitude the (0,1) mode representing the two-dimensional effects is of comparable magnitude and behavior (Fig. 22(a)) for the linear and serpentine geometry cases. However, the three dimensional behavior (i.e., the (1,1) mode) varies, depending on which actuator geometry is employed (Fig. 22(b)). When serpentine geometry actuators are used, three-dimensional behavior is directly excited by the actuator, but for the linear geometry, this behavior starts

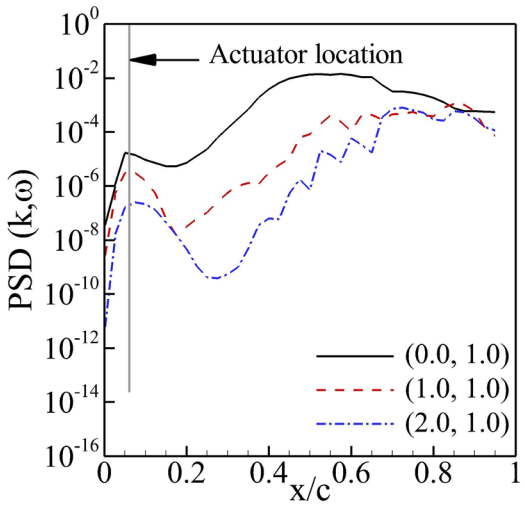

FIG. 21. Magnitude of the fundamental frequency (St = 5.0) modes across a number spatial frequencies for the quarter serpentine geometry.

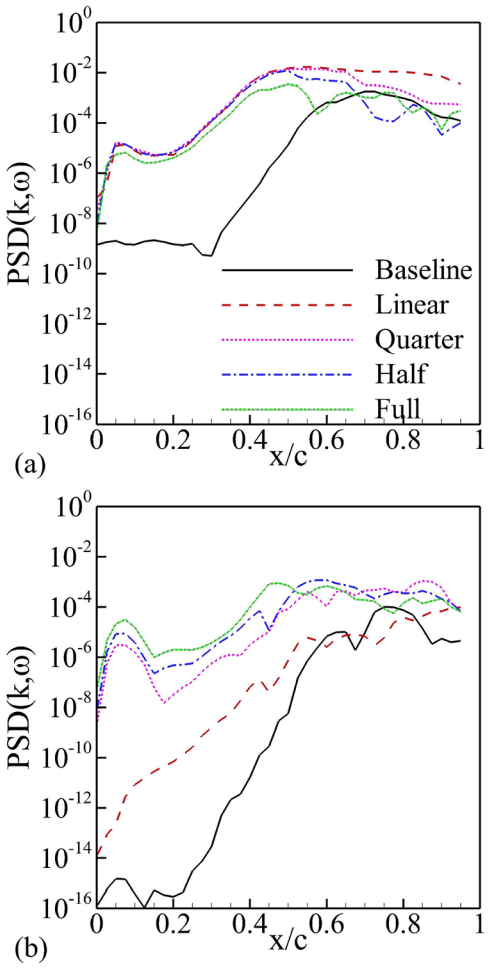

FIG. 22. Magnitude of the (a) spanwise constant (0,1) and (b) fundamental spatial (1,1) Fourier modes at the fundamental temporal frequency.

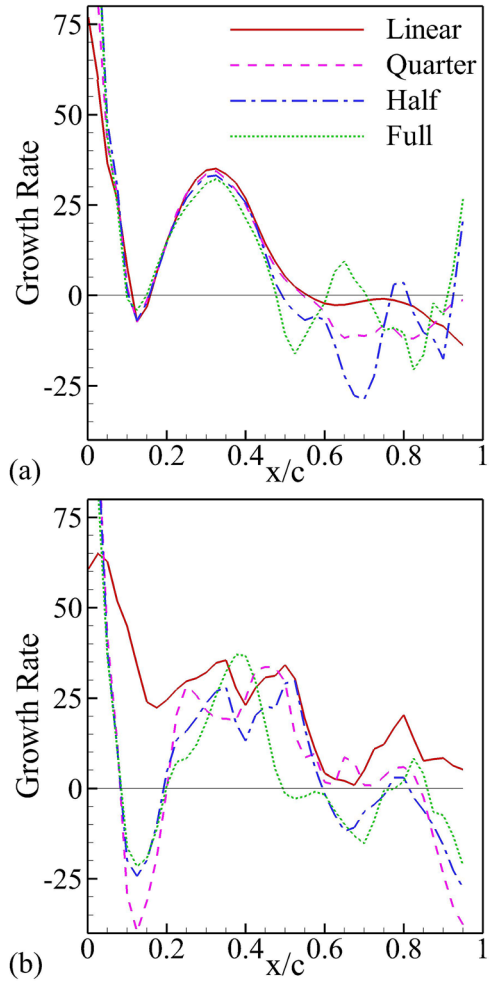

FIG. 23. Exponential growth rates of Fourier modes for (a) spanwise constant (0,1) and (b) fundamental spatial (1,1) Fourier modes at the fundamental temporal frequency.

off as being very small near the leading edge of the airfoil, and slowly grows as it is convects downstream. Eventually, both the two-dimensional and three-dimensional effects saturate in magnitude due to non-linearities in the flow.

Comparing the spatial growth rates (defined as the negative of the logarithmic derivative) of the (0,1) and (1,1) modes (Fig. 23), the growth rates of these modes seem to be relatively close for the linear and serpentine actuators from $x/c = 0.05$ to $x/c = 0.5$ for the (0,1) mode and $x/c = 0.2$ to $x/c = 0.4$ for the (1,1) mode. The similarities in the growth rates would indicate that the growth rate of these flow features is not as strongly dependent on the excitation introduced to the flow as it is dependent on the baseflow and its stability properties.

VI. CONCLUSIONS

In order to show the versatility of serpentine class of plasma actuators, two different flow control applications have been examined. In the first, this type of actuator has been studied in order to generate vortical streaks in a zero pressure gradient boundary layer. In the second example, these actuators have been employed to accelerate the transition of a low Reynolds number airfoil flow in order to make it more robust against separation.

A majority of air vehicles undergo widely varying flow conditions in a single flight (i.e., high lift, low speed take-offs, and landings, along with lower lift, high speed cruising), and the requirements for flow control change along with the flow conditions. As serpentine geometry plasma actuators are able to excite several different physical mechanisms depending on how they are operated, there could be potential usage for a fixed actuator under most, if not all stages of an air vehicle's flight. Due to its versatility under varying conditions, this class of plasma actuators may be able to replace other flow control devices that are beneficial only during individual stages of a flight and detrimental during others. As different actuators all require their own power supplies and controllers, employing multiple flow control devices on a single vehicle may be undesirable due to the additional weight of each actuator and its associated equipment. Consolidating the different flow control competencies into a single actuator should minimize the weight of equipment that must be carried on board in order to perform flow control and minimize the negative side effects of control devices that are only useful during individual portions of an air vehicle's flight.

The present results, in addition to other studies in existing literature, indicate that serpentine geometry plasma actuators can be useful under a wide variety of flow conditions. Further work on this topic may shed light on the bounds of control authority that these actuators possess under a wider set of flow conditions. Should the capabilities of this type of actuator be sufficient, they may pose themselves as being useful for larger scale applications, and enable more efficient flow control for air vehicles. Ultimately, this could lead to more efficient, less costly flight.

ACKNOWLEDGMENTS

This work was partially supported by AFOSR grant FA9550-09-1-0372 monitored by Dr Douglas Smith. The authors would like to thank Dr. Miguel Visbal of the Air Force Research Laboratory for the use of the code FDL3DI. The first author would also like to thank the University of Florida's Graduate School Fellowship Award, which provided partial support for this study.

[1]L. N. Cattafesta and M. Sheplak, "Actuators for active flow control," Ann. Rev. Fluid Mech. **43**, 247–272 (2011).
[2]E. Moreau, "Airflow control by non-thermal plasma actuators," J. Phys. D: Appl. Physi. **40**, 605–636 (2007).
[3]T. C. Corke, C. L. Enloe, and S. P. Wilkinson, "Dielectric barrier discharge plasma actuators for flow control," Ann. Rev. Fluid Mech. **42**, 505–529 (2010).
[4]M. R. Visbal, "Strategies for control of transitional and turbulent flows using plasma-based actuators," Int. J. Comput. Fluid Dyn. **24**(7), 237–258 (2010).
[5]D. P. Rizzetta and M. R. Visbal, "Large-eddy simulation of plasma-based turbulent boundary-layer separation control," AIAA J. **48**, 2793–2810 (2010).
[6]J. R. Roth, D. M. Sherman, and S. P. Wilkinson, "Electrohydrodynamic flow control with a glow-discharge surface plasma," AIAA J. **38**, 1166–1172 (2000).

[7]D. M. Schatzman, M. David, and F. O. Thomas, "Turbulent boundary-layer separation control with single dielectric barrier discharge plasma actuators," AIAA J. **48**(8), 1620–1634 (2010).
[8]D. Greenblatt, C. Y. Schuele, D. Roman, and C. O. Paschereit, "Dielectric barrier discharge, flow control at very low flight Reynolds numbers," AIAA J. **46**(6), 1528–1541 (2008).
[9]D. P. Rizzetta and M. R. Visbal, "Numerical investigation of plasma-based flow control for transitional highly loaded low-pressure turbine," AIAA J. **45**(10), 2554–2564 (2007).
[10]D. P. Rizzetta and M. R. Visbal, "Numerical investigation of plasma-based control for low-Reynolds number airfoil flows," AIAA J. **49**(2), 411–425 (2011).
[11]S. Roy and C. C. Wang, "Bulk flow modification with horseshoe and serpentine plasma actuators," J. Phys. D: Appl. Phys. **42**, 032004 (2009).
[12]C. Wang, R. Durscher, and S. Roy, "Three-dimensional effects of curved plasma actuators in quiescent air," J. Appl. Phys. **109**, 083305 (2011).
[13]A. Santhanakrishnan and J. Jacob, "Flow control with plasma synthetic jet plasma actuators," J. Phys. D: Appl. Phys. **40**, 637–651 (2007).
[14]R. Durscher and S. Roy, "Three-dimensional flow measurements induced from serpentine plasma actuators in quiescent air," J. Phys. D: Appl. Phys. **45**, 035202 (2012).
[15]D. P. Rizzeta, M. R. Visbal, and P. E. Morgan, "A high-order compact finite-difference scheme for large-eddy simulations of active flow control," Prog. Aerospace Sci. **44**, 397–426 (2008).
[16]K. P. Singh and S. Roy, "Force approximation for a plasma actuator operating in atmospheric air," J. Appl. Phys. **103**, 13305 (2008).
[17]K. Butler and B. Farrell, "Three dimensional optimal pertubations in viscous shear flow," Phys. Fluids **4**(8), 1637–1650 (1992).
[18]P. Andersson, M. Berggren, and D. S. Henningson, "Optimal disturbances and bypass transition in boundary layers," Phys. Fluids **11**(1), 134–150 (1999).
[19]K. J. A. Westin, A. V. Boiko, B. G. B. Klingmann, V. V. Kozlov, and P. H. Alfredsson, "Experiments in a boundary layer subjected to free stream turbulence. Part 1. Boundary layer structure and receptivity," J. Fluid Mech. **281**, 193–218 (1994).
[20]P. Andersson, L. Brandt, A. Bottaro, and D. S. Henningson, "On the breakdown of boundary layer streaks," J. Fluid Mech. **428**, 29–60 (2001).
[21]J. H. M. Fransson, A. Talamelli, L. Brandt, and C. Cossu, "Delaying transition to turbulence by a passive mechanism," Phys. Rev. Lett. **96**, 064501 (2006).
[22]D. Gaitonde, "Three-dimensional plasma-based flow control simulations with high-fidelity coupled first-principles approaches," Int. J. Comput. Fluid Dyn. **24**(7), 259–279 (2010).
[23]D. Greenblatt and I. J. Wygnanski, "The control of flow separation by periodic excitation," Prog. Aerospace Sci. **36**, 487–545 (2000).
[24]J. C. R. Hunt, A. Wrap, and P. Moin, "Eddies, stream and convergence zones in turbulent flows," Center For Turbulence Research Report CTR-S88, 1998.
[25]M. C. Galbraith and M. R. Visbal, "Implicit large eddy simulation of low Reynolds number transitional flow past the SD7003 airfoil," AIAA Paper 2010-4737, 2010.
[26]M. V. Ol, B. R. McAuliffe, E. S. Hanff, U. Scholz, and C. Kahler, "Comparison of laminar separation bubble measurements on a low Reynolds number airfoil in three facilities," AIAA Paper 2005-5149, 2005.